Locating Nuclear Explosions at the Chinese Test Site near Lop Nor

Vipin Gupta[a]

This paper describes how commercial satellite imagery was used along with teleseismic P-wave arrival time data to locate 21 Chinese nuclear tests. The results include a set of refined location estimates for atmospheric and underground tests as well as error vectors from the initial seismic location estimates to the refined location estimates. The analysis of the results provided new information on Chinese nuclear testing patterns which have been used to revise China's testing history and assist the satellite monitoring of the test site. The paper concludes with an evaluation of commercial satellite imaging for monitoring nuclear tests and an assessment of the implications of the results with respect to the verification of a comprehensive test ban (CTB).

INTRODUCTION

In contrast with the French, Russian, and US nuclear test sites, the Chinese test site near Lop Nor continues to be used for nuclear explosive tests. It has gained worldwide notoriety as the sole operational test site, attracting the attention of the other four nuclear weapons states as well as the rest of the international community. Since 1992, several states and non-governmental organizations have carefully watched the activities at the Chinese test site to determine China's future testing intentions, estimate the capabilities of China's modernized nuclear arsenal, and gain insight on China's diplomatic position regarding the nuclear testing moratoria and comprehensive test ban treaty.[1]

The increased interest in Chinese nuclear testing coincides with the publication of several studies that provide us with a greater understanding of the

geology and nuclear testing history at the site. J. Matzko of the US Geological Survey published the most detailed description to date of the geological structures and rock types at the test site.[2] His findings are based on the analysis of several articles that were published in Chinese technical journals. R. Norris *et al.* of the Natural Resources Defense Council published the most up-to-date history of Chinese nuclear testing.[3] Their book includes details on the establishment of the test site near Lop Nor, descriptions of nuclear tests that represented significant technological achievements, and a list of facts on each Chinese nuclear test through 1993. Adding to the contribution by R. Norris *et al.*, J. Murphy of S-Cubed refined the seismic yield estimates of 11 Chinese underground tests.[4] His yield estimates were derived from network-averaged, P-wave frequency spectra from the explosions.[5]

In addition to yield estimation, two recent studies have also been conducted to locate the detonation points of past Chinese nuclear tests accurately. One of the studies — conducted by Douglas *et al.* of the UK Atomic Weapons Establishment (AWE) — relied on Matzko's geological analysis and teleseismic P-wave arrival time data to refine the seismic location estimates of Chinese nuclear tests that were reported in the International Seismological Center (ISC) bulletins through 1988.[6] The other study — conducted by the author — relied on commercial satellite imagery and teleseismic P-wave arrival time data.[7] The analysis of the satellite imagery pinpointed the location of two Chinese tests which were used as geographic reference points to refine the seismic location estimates of the remaining Chinese nuclear tests that were reported in the ISC and NEIS (National Earthquake Information Service) bulletins through 1992.

This paper describes how commercial satellite imagery was used along with seismic data to locate 21 Chinese nuclear tests. The results include a set of refined location estimates for atmospheric and underground nuclear tests as well as error vectors from the ISC and NEIS locations to the new location estimates. The magnitude of the systematic and random errors provide valuable insight on the utility of ISC and NEIS data for pointing space-based sensors at nuclear detonation points on the ground. The refined location estimates also reveal new facts on Chinese nuclear testing patterns. These previously unknown patterns proved useful in forecasting the borehole orientation and yield range of two Chinese nuclear tests — on 25 September 1992 and 5 October 1993 — that commercial satellite imagery indicated were under preparation.[8]

For future monitoring of the Chinese test site, the improved location estimates of past Chinese tests can be used to reduce the size of the ground area that needs to be imaged and analyzed for new nuclear testing activity. The

results revealed that approximately 200 square kilometers of the 100,000 square kilometer test site is still used for nuclear testing. This large reduction in the area of interest is likely to prove particularly useful for the acquisition of commercial high-resolution images of the test site. Since such imagery is priced on a per square kilometer basis, the total cost can be dramatically reduced by minimizing the size of the area of interest.[9]

The next section of this paper describes the seismic data that was used in this study and the algorithm, the Joint Epicenter Determination (JED), for refining seismic location estimates. The third section details the processing and analysis of Landsat Multispectral Scanner (MSS) and Large Format Camera (LFC) imagery for the detection, identification, and location of the 3 October 1984 detonation point. The geographic position of this underground test was used as one of two reference points for the JED. The fourth section presents the results as well as an analysis of the results. The analysis provided new information on Chinese nuclear testing patterns which have been used to revise China's testing history and assist the satellite monitoring of the test site. The paper concludes with an evaluation of commercial satellite imaging for monitoring nuclear tests and an assessment of the implications of the results with respect to the verification of a comprehensive test ban (CTB).

SEISMIC LOCATION ESTIMATION OF CHINESE NUCLEAR TESTS

Seismic Data

Twenty-three atmospheric tests and fifteen underground tests are known to have been conducted at the Chinese test site between 1964 and 1992.[10] Of these known tests, seven atmospheric tests and fourteen underground tests were detected seismically and reported in the ISC and NEIS bulletins.[11] The seven atmospheric tests were conducted at a sufficiently low scaled height of burst to generate a detectable seismic signal.[12]

Table 1 provides the ISC and NEIS estimates of the origin time, geographic location, and body wave magnitude (m_b) for the 21 nuclear tests. The table also lists the best available yield estimates, the number of stations that reported each seismic event, and the type of nuclear test that was conducted.

Table 1: Seismic events reported in the ISC and NEIS bulletins that were generated by nuclear explosions at the Chinese nuclear test site.

Date	Time (GMT)	Latitude	Longitude	m_b	Yield[13] (kt TNT)	Number of Stations	Type of Test
17 Jun 67	00:19:09.8	40.800 N	89.400 E	4.7	3300	18	Atmospheric
22 Sep 69	16:14:58.9	41.350 N	88.330 E	5.2	19.2	95	Underground
29 Sep 69	08:40:26.2	40.720 N	89.300 E	4.5	3000	5	Atmospheric
14 Oct 70	07:29:58.9	40.920 N	89.400 E	4.6	3400	9	Atmospheric
27 Jun 73	03:59:45.9	40.662 N	89.675 E	4.8	2000-3000	33	Atmospheric
17 Jun 74	05:59:52.5	40.552 N	89.463 E	4.5	200-1000	9	Atmospheric
27 Oct 75	00:59:59.2	41.433 N	88.400 E	5.0	2.5	58	Underground
17 Oct 76	05:00:03.8	41.644 N	88.210 E	4.9	2.6	56	Underground
17 Nov 76	06:00:17.6	40.782 N	89.661 E	4.6	~ 4000	25	Atmospheric
14 Oct 78	01:00:02.3	41.419 N	88.663 E	4.9	3.4	76	Underground
16 Oct 80	04:30:28.9	41.038 N	89.990 E	4.4	200-1000	6	Atmospheric
04 May 83	05:00:02.0	41.627 N	88.313 E	4.5	~ 1	9	Underground
06 Oct 83	09:59:58.0	41.526 N	88.721 E	5.5	14.9	215	Underground
03 Oct 84	05:59:57.9	41.543 N	88.672 E	5.4	9.1	172	Underground
19 Dec 84	06:00:02.8	41.624 N	88.218 E	4.7	1.3	43	Underground
05 Jun 87	04:59:58.5	41.547 N	88.720 E	6.2	250	529	Underground
29 Sep 88	07:00:02.0	41.524 N	88.154 E	4.6	2.5	25	Underground
26 May 90	07:59:57.8	41.566 N	88.688 E	5.4	11.5	219	Underground
16 Aug 90	04:59:57.6	41.564 N	88.770 E	6.2	189	513	Underground
21 May 92•	04:59:57.2	41.549 N	88.835 E	6.6	650	262	Underground
25 Sept 92•	07:59:58.4	41.780 N	88.413 E	5.1	~ 8	37	Underground

• – NEIS data

Calculation of the Nuclear Test Location

For each nuclear test shown in Table 1, the ISC and NEIS bulletins list the arrival time for the short-period (.5–5 Hz) P-wave at each seismic station that reported the event. To locate each test, these arrival times are used to solve for four unknowns — latitude, longitude, depth, and origin time (i.e., time of detonation). The calculation requires an empirically derived model of seismic wave propagation known as a "travel time curve" or "travel time table." This model tabulates the time it takes for seismic waves to traverse various distances. The Jeffreys and Bullen global travel time table was used in this study.[14] This table is most applicable for locating seismic events where the distance from the detonation point to each receiving station is greater than 2000 km — teleseismic distances. Teleseismic P-wave trajectories are simulated using a global model since the path is not confined to the crust and upper mantle where the propagation properties are governed by local and regional geological structures (see Figure 1).

The location of a seismically detected nuclear test is calculated iteratively. The algorithm requires solving a set of linearized equations where each equation represents the trajectory from the detonation point to a specific seismic station.[15] An initial guess is made on the location of the detonation point. Using the initial guess and the travel time tables, the predicted arrival times are calculated for each of the stations that detected the nuclear test. Applying a least squares approach, the location of the detonation point is varied to minimize the cumulative differences between the predicted and actual arrival times. Using refined location estimates, the process is continued successively until the cumulative error approaches an asymptotic value.

The solution contains random and systematic errors. The random error can be significantly reduced if 10-20 seismic stations distributed 360° around the detonation point record the event and if the arrival times are measured accurately.[16] Systematic location errors are due to deviations between the travel time model of seismic wave propagation and the actual Earth's behavior. The deviations can be attributed to local and regional propagation peculiarities under the explosive source and distant seismic receiver as well as large-scale anomalies within the mantle.[17] The magnitude and direction of the systematic error vary according to the geographic area. The magnitude of the systematic error component is generally larger than the magnitude of the random error component. From the existing global network of seismic stations, the magnitude of systematic error is estimated to be around 20 km with random error up to 10 km.[18] The magnitudes for both errors increase by a factor of two or three for weak seismic events ($m_b < 4.5$) detected by a small number of stations characterized by a limited azimuthal distribution about the detonation point.
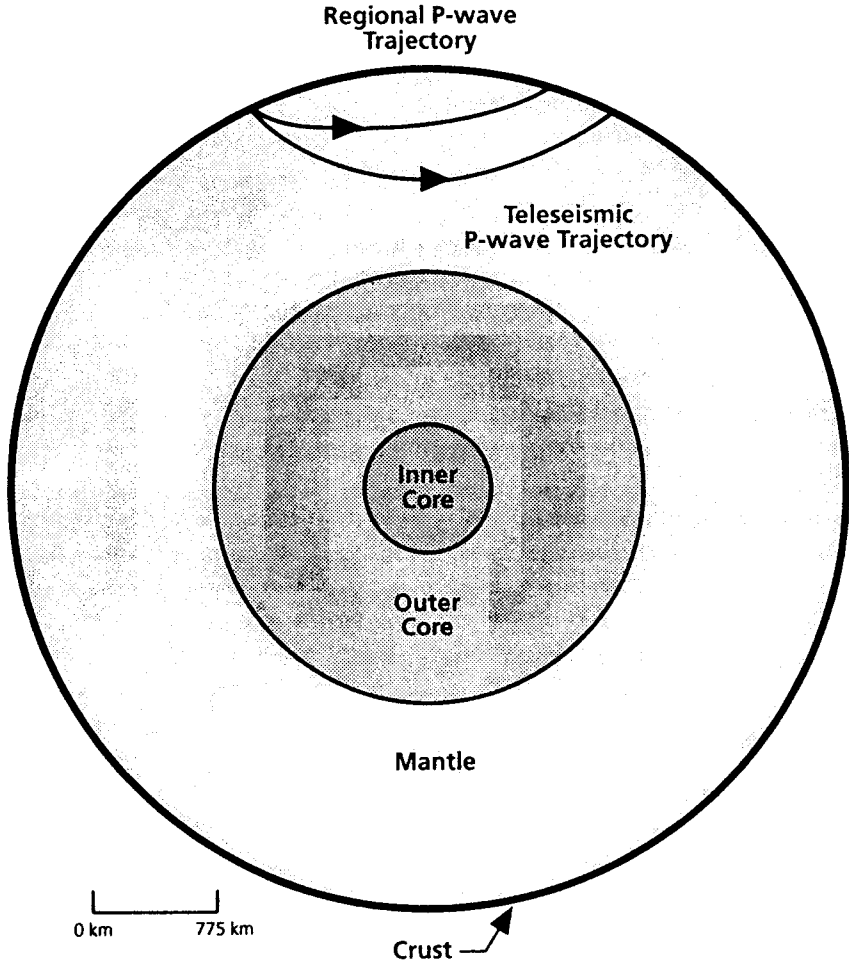
Figure 1: P-wave trajectories at regional (< 2000 km) and teleseismic (> 2000 km) distances. The velocity profile varies according to depth so the path bends in accordance with Snell's Law.

For seismically-detected nuclear explosions conducted within a specific test site, the systematic location errors can be reduced using a technique known as the Joint Epicenter Determination (JED). The JED calculates the location of multiple nuclear tests simultaneously relative to the fixed epicenter and origin time of at least one nuclear explosion in the same area.[19] If the geographic location of the reference explosions can be determined through nonseismic means, the JED can effectively calibrate the seismic location esti-

mates, reducing the systematic location errors and providing an absolute rather than relative location estimate for each nuclear test in the dataset. It can also provide a list of travel time corrections for each seismic station. The station corrections compensate for the observed differences between the travel time model and the actual Earth's behavior. For future nuclear tests in the same area, the corrections can be used to reduce the systematic location error without applying the JED.

PROCESSING AND ANALYSIS OF COMMERCIAL SATELLITE IMAGERY

To apply the JED and refine the seismic location estimates of the Chinese nuclear tests in Table 1, the geographic location of at least one of the listed tests had to be determined through nonseismic means. A review of Chinese technical and nontechnical literature failed to come up with the location of any of the 21 nuclear tests, although it did provide valuable clues on the relative location of four underground nuclear explosions.[20] A review of the US and UK literature also failed to come up with a single usable reference explosion. Given the absence of published geographic data on the Chinese test site, there was only one other viable source for the required information — commercial satellite imagery.

A variety of images were obtained and analyzed in an effort to detect, identify, and pinpoint past Chinese nuclear tests. The images were acquired by Landsat-1 Multispectral Scanner (MSS), Large Format Camera (LFC), SPOT-1 panchromatic, SPOT-1 multispectral, Landsat-4 Thematic Mapper (TM), and ALMAZ-1 synthetic aperture radar (SAR). The analysis of the images acquired by Landsat-1 MSS and LFC provided the locations of two nuclear tests that were used as reference events for the JED. One of the pinpointed tests was the 27 June 1973 atmospheric shot located at $40.7985\pm.0005°$ N, $89.8091\pm.0005°$ E. That test was detected, identified, and located in a digital merge of Landsat-1 MSS imagery acquired on 12 June 1973 (t–15 days) and 30 June 1973 (t+3 days).[*] The other test was the 3 October 1984 underground shot. That test was found through the analysis of an

---

[*] For the technical details on the processing and interpretation of the 12 June 1973 and 30 June 1973 MSS images, see Vipin Gupta, "Using Landsat-1 MSS Imagery to Locate the 27 June 1973 Nuclear Explosion at the Chinese Nuclear Test Site near Lop Nor," in preparation. See also Ref. 7: Gupta, *A Remote Sensing and Photogrammetric Study of the Chinese Nuclear Test Site*, pp. 155-180.

LFC image acquired on 7 October 1984 and a Landsat-1 MSS image acquired on 4 October 1972.

Search for the 3 October 1984 Detonation Point

On 3 October 1984 at 0600 GMT, China conducted an underground nuclear test that generated a relatively strong seismic signal (m_b=5.4). On 5 October 1984 at 0203 GMT, the Space Shuttle Challenger was launched into low Earth orbit carrying the Large Format Camera. Orbiting at an inclination angle of 57°, the LFC began its preprogrammed sequence of image acquisitions using natural color, infrared color, and panchromatic film. On 7 October 1984 at 0731 GMT, the LFC acquired panchromatic stereo images of the Chinese test site – just four days, one hour, and 31 minutes after China conducted an underground nuclear test there. LFC image 496 and 497 were acquired at an altitude of 266.2 km and 266.0 km respectively. The images covered a 200 x 400 km area, including the ISC and NEIS locations of the 21 Chinese nuclear tests listed in Table 1.

The ISC estimated the location of the 3 October 1984 test to be at 41.54±0.15° N, 88.67±0.019° E. This estimate was selected as the center point for the search. Based on earlier seismic studies of location bias, the magnitude of the systematic error in the ISC estimate was assumed to be on the order of 20 km. With the direction of the systematic error unknown, this translated to a search area on the order of 1200 square kilometers. The search concentrated on an area of this size within the northwest quadrant (76.8 km x 102.4 km) of a processed LFC orthoimage — an image without terrain-height distortions. Processed to a 50 meter pixel grid interval, the orthoimage was derived from LFC image 496 and the digital elevation model that was produced from the LFC stereo pair.[†]

The technical objective of the search was to find surface features in the LFC orthoimage that could be established as distinct changes to the natural environment. The detection of changes in the area required a reference image for comparison. An image acquired shortly before the test would have been ideal. Unfortunately, the catalog of available commercial satellite images did

---

[†]   For technical details on the production of the LFC orthoimage, see Gupta, *A Remote Sensing and Photogrammetric Study of the Chinese Nuclear Test Site*, pp. 115-154.
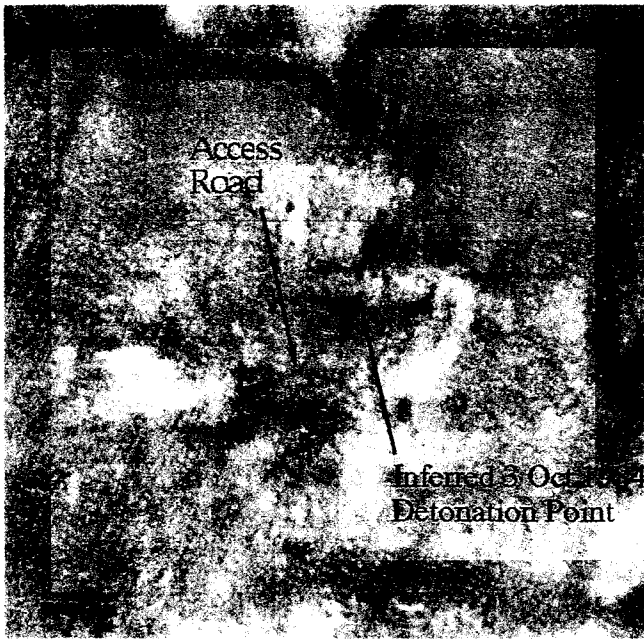
Plate 1 : Inferred 3 October 1984 detonation point shown in ratio image of MSS synthetic band (10/4/72) and LFC orthoimage (10/7/84). Image extent: 13.55 km x 13.30 km.

not contain such a "pre-test" image. As a substitute, the Landsat-1 MSS scene acquired on 4 October 1972 was used as the reference image. This scene was the oldest available satellite image of the area.

In order to use this reference image for change detection, the MSS image was radiometrically corrected for atmospheric scattering, converted to a panchromatic band, geometrically registered to the LFC orthoimage, resampled to a 50 meter pixel grid interval, and digitally merged with the LFC orthoimage through temporal band ratioing (see Appendix A). The ratio image showed the nature and scale of the surface changes that occurred between the two image acquisitions. Pixels that represented little or no change between 4 October 1972 and 7 October 1984 were shown in medium tones of gray. Pixels that represented surface changes were depicted either as dark or light where the magnitude of the change increased as the ratio approached 0 (pure black) or 255 (pure white).

Most of the ratio image was texturally uniform since the division removed spatial variations in albedo and since much of the area was unaltered over the 12 year time interval. However, two distinct changes were found — an access

road ending at a large blemish (see plate 1). The road and blemish were depicted as dark in the image which indicated a temporal increase in the surface reflectivity (see equation A-5). The blemish was located in flat terrain and had a maximum extent of 489±35 meters.[21]

In the LFC orthoimage, the same features were found to have higher albedo than the adjacent surroundings. The high albedo was attributed to the removal of natural obstacles (e.g. boulders, outcrop) and the construction of smoothed surfaces to facilitate road transport.[22] The texture of the features was not uniform and contrasted with the paved roads in the area.[23] This strongly suggested that the large blemish and access road were unpaved.

At known test sites, it is routine to construct access roads ending at selected sites for nuclear tests in deep vertical shafts. Underground nuclear tests require large-scale ground activity to prepare for the test as well as to analyze the results. This activity involves pre-test and post-test drilling, device emplacement, borehole capping, and the deployment of instrumentation including relay cables.[24] It is reasonable to assume the Chinese have to undertake similar tasks for vertical shaft tests. It is also reasonable to expect such activity to disturb the surface, thereby altering its reflectance characteristics.

Since the temporal features found in the ratio image were similar in coarse appearance to vertical shaft sites at other nuclear testing grounds and since the features were located within the general vicinity of ISC and NEIS location estimates of known Chinese tests, it was reasonable to infer that the blemish was indeed the detonation point for a vertical shaft test. Evidence from a Chinese technical paper by Y. Che gave more credence to this inference by linking the location of the detected blemish to the location of an underground nuclear test described in Che's paper (see Appendix B).

Considering the magnitude and extent of the surface change shown in Plate 1, the prominence of the detonation point with respect to the nearby surroundings (see Figure B.1), and the fact that the LFC image was acquired just days after an underground test in the area, it was possible to go one step further and deduce that the surface blemish contained the 3 October 1984 detonation point. No comparable features were found elsewhere in the ratio image which can be attributed to the cessation of activity at older detonation points and seasonal winds that gradually erase anthropogenic changes to the surface.[25]

The blemish itself did not reveal the exact location of the 3 October 1984 borehole. The spatial resolution of the LFC orthoimage was not high enough to detect the shaft or support infrastructure. Nor were there any detectable surface effects, such as spalling or subsidence cratering, from the test itself. The

detonation point was assumed to be located at the eastern corner of the blemish since it was not adjacent to the access road and since the rest of the blemish fanned out west of the point.[26] That position appeared sufficiently remote for isolating near-source shock effects and potential subsidence cratering. The geographic location of this point is $41.5713 \pm .0005°$ N, $88.7216 \pm .0005°$ E. That location is 5.53 km northeast of the ISC location estimate for the 3 October 1984 test (see Figure 5 and Table D.1).

RESULTS FROM THE JOINT EPICENTER DETERMINATION

Application of the JED

By deducing the latitude and longitude of the 3 October 1984 test and assuming the depth of burial to be at the Earth's surface, it was possible to calculate the 3 October 1984 detonation time.[‡] The detonation time was needed as a fixed time reference for the JED. The problem was solved directly rather than iteratively since the detonation time was the only unknown. Seismic stations with source-to-receiver distances less than 20° or greater than 95° were excluded since the Jeffreys-Bullen travel time tables did not accurately model regional propagation nor propagation through the Earth's core (see Figure 1).[27] At an assumed depth of 0 km, the detonation time was found to be $05:59:57.99 \pm 0.13$ GMT.

This detonation time, along with the geographic locations of the 3 October 1984 and 27 June 1973 tests, were fixed for the JED. As with the calculation of the 3 October 1984 detonation time, all seismic stations in the JED dataset with source-to-receiver distances less than 20° or greater than 95° were excluded. In addition, poor station readings from an initial JED run (residuals > 2σ) were removed from the dataset. The poor station readings can be attributed to instrument faults and incorrect data interpretation. After sifting out these readings, the final JED run was executed.

The JED provided refined location estimates for 21 Chinese nuclear tests (see Table 2). A plot of the refined locations revealed the existence of four distinct testing zones within the Chinese test site — three for underground tests and one for high-yield, atmospheric tests.[28] The four testing zones were also

---

‡ The seismic propagation model did not account for surface topography; the explosive source and the seismic stations were assumed to be located on the surface of a spheroidal Earth.

Table 2: JED results for nuclear explosions at the Chinese test site.

| Date	Time (GMT)	Latitude	Longitude	Test Zone	Borehole Orientation	Type of Test
17 Jun 67	00:19:08.20	40.744 N	89.775 E	D	na	Atmospheric
22 Sep 69	16:14:59.21	41.376 N	88.318 E	B	Tunnel	Underground
29 Sep 69	08:40:21.36	40.722 N	89.515 E	D	na	Atmospheric
14 Oct 70	07:29:56.91	40.520 N	89.779 E	D	na	Atmospheric
27 Jun 73	03:59:46.29	40.7985 N	89.8091 E	D	na	Atmospheric
17 Jun 74	05:59:52.72	40.518 N	89.619 E	D	na	Atmospheric
27 Oct 75	00:59:58.23	41.375 N	88.326 E	B	Tunnel	Underground
17 Oct 76	04:59:58.80	41.708 N	88.370 E	A	Tunnel	Underground
17 Nov 76	06:00:12.70	40.696 N	89.627 E	D	na	Atmospheric
14 Oct 78	00:59:58.01	41.523 N	88.722 E	C	Shaft	Underground
16 Oct 80	04:30:29.67	40.719 N	89.651 E	D	na	Atmospheric
04 May 83	04:59:57.82	41.679 N	88.368 E	A	Tunnel	Underground
06 Oct 83	09:59:58.05	41.538 N	88.714 E	C	Shaft	Underground
03 Oct 84	05:59:57.99	41.5713 N	88.7216 E	C	Shaft	Underground
19 Dec 84	05:59:58.34	41.737 N	88.425 E	A	Tunnel	Underground
05 Jun 87	04:59:58.26	41.518 N	88.713 E	C	Shaft	Underground
29 Sep 88	06:59:57.97	41.768 N	88.380 E	A	Tunnel	Underground
26 May 90	07:59:57.94	41.569 N	88.701 E	C	Shaft	Underground
16 Aug 90	04:59:57.70	41.514 N	88.739 E	C	Shaft	Underground
21 May 92	04:59:57.45	41.513 N	88.774 E	C	Shaft	Underground
25 Sept 92	07:59:58.47	41.716 N	88.336 E	A	Tunnel	Underground

na – not applicable
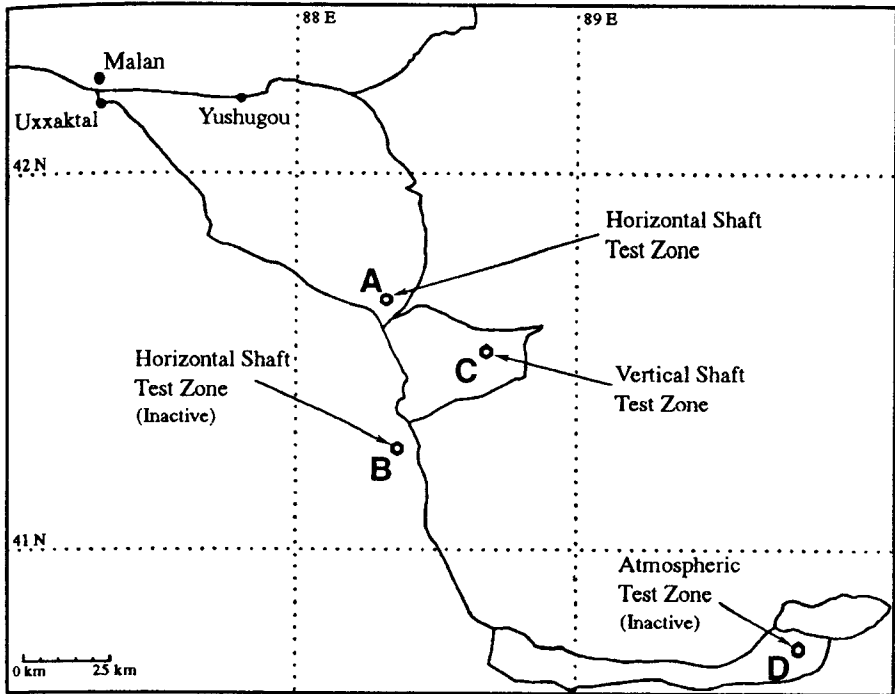
Figure 2: Layout of the Chinese nuclear test site.

resolvable in the JED results obtained by Douglas *et al.* of the UK Atomic Weapons Establishment (AWE),[29] although the AWE test locations differ from the locations in Table 2 to varying degrees depending on the test zone (see Appendix C).

Only two test zones are still used for nuclear explosives testing. Figure 2 shows a map of the entire test site that includes the general location of the four test zones. The map also shows the location of Malan, the scientific support city, and the generalized road network from the 1:1,000,000 scale Operational Navigational Chart produced by the US Defense Mapping Agency.

Of the three test zones used for underground nuclear explosions, two were used for tunnel shots. The borehole orientation for each underground nuclear test was inferred from a plot of the 95 percent confidence JED error ellipses onto the LFC digital elevation model (see Table 2). If the terrain within the 95 percent confidence error ellipse was flat, the underground test was inferred to have been conducted in a vertical shaft. If the terrain within the error ellipse was mountainous, the test was inferred to have been conducted in a tunnel.

Figures 3-5 show how the seismic locations for the Chinese nuclear tests converged to the four separate testing zones (see Appendix D for the tabulated results). The graphs show the ISC/NEIS location estimates for each explosion and the displacement line to the JED location estimate. The ISC/NEIS locations are labeled by the year of the test. In Figures 4 and 5, the ISC/NEIS locations are labeled by the month and year of the test if more than one underground test was conducted in the calendar year. Note that Figure 3 is plotted on a different scale from Figures 4 and 5. To check for consistency in the JED results on location errors, the displacement distances and the areal coverage of the JED error ellipses were analyzed in relation to the body wave magnitude (m_b). The displacement distance was a measure of the systematic error while the area of the error ellipse was a measure of the random error.

Figure 6 shows the displacement distances in relation to the strength of the seismic event. The plot shows a significant decrease in the systematic error as the m_b increases from 4.0 to 5.0. For $m_b > 5.0$, the magnitude of the systematic error was insensitive to the strength of the event. This result is consistent with the conclusions from other seismic studies on event location. For relatively strong seismic signals ($m_b > 5.0$) detected by 10-20 well distributed stations, teleseismic location accuracy is fairly insensitive to the use of greater numbers of seismic stations.[30]

Figure 7 shows the area of the error ellipses in relation to the strength of the seismic event. As expected statistically, the area varied inversely with the body wave magnitude. For weak events detected by a small number of seismic stations (< 10), the uncertainty in the event location was significantly larger than the uncertainty for stronger events.
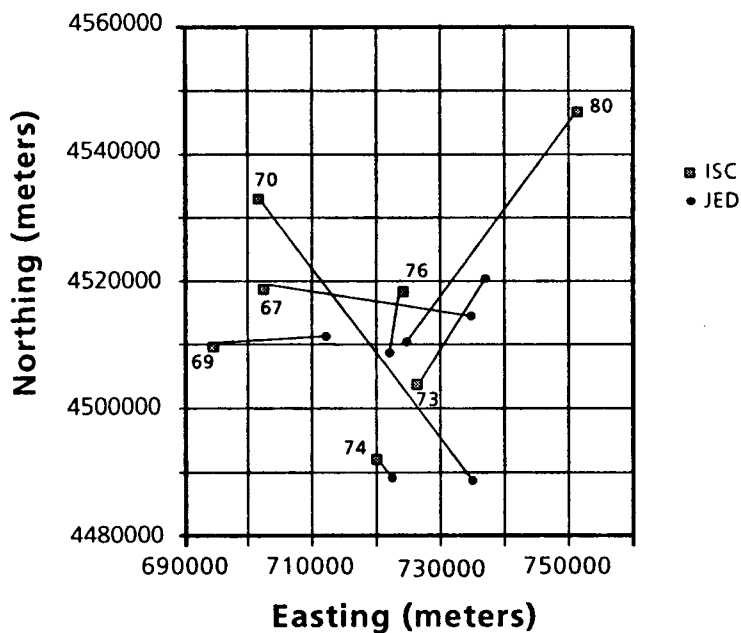
Figure 3: ISC and JED location estimates for high-yield, atmospheric tests in zone D (UTM grid units). The refined location of the 27 June 1973 detonation point was derived from Landsat-1 MSS imagery.
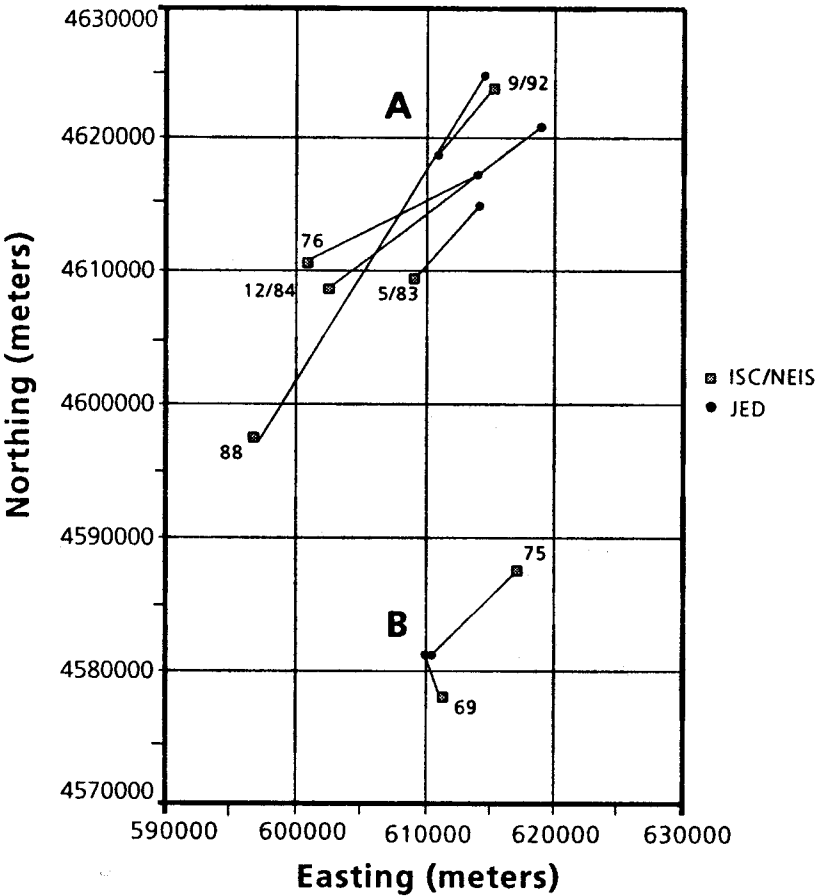
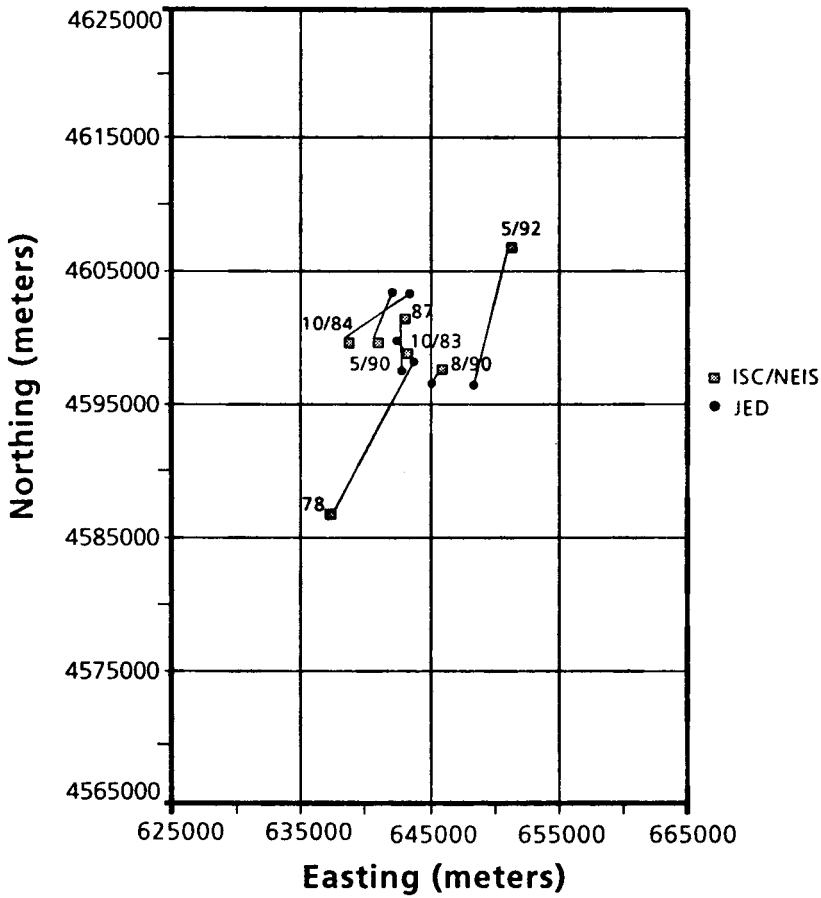**Figure 4:** ISC/NEIS and JED location estimates for tunnel tests in zones A and B (UTM grid units).

Figure 5: ISC/NEIS and JED location estimates for vertical shaft tests in zone C (UTM grid units). The refined location of the 3 October 1984 detonation point was derived from Landsat-1 MSS imagery and LFC imagery.
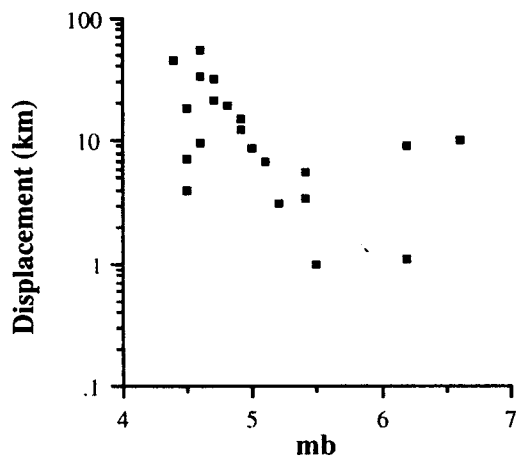
Figure 6: Displacement distance in relation to the body wave magnitude.
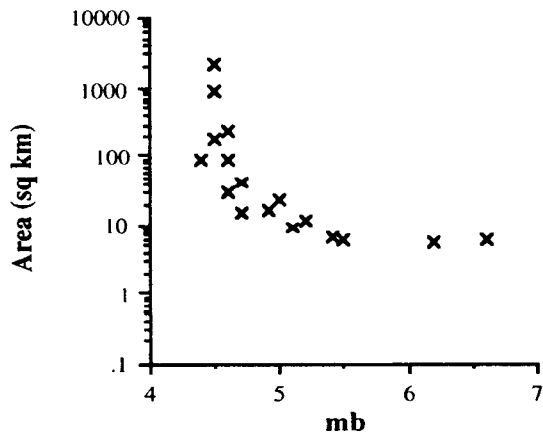

Figure 7: Area of 95 percent confidence error ellipses in relation to the body wave magnitude.

DEDUCTIONS FROM THE JED RESULTS

The identification of the four test zones revealed that only a small portion of the test site was used for nuclear explosives testing. The high-yield, atmospheric test range — zone D (40° 45' N, 89° 30' E) — was last used on 16 October 1980. Zone B (41° 23' N, 88° 18' E) was used for China's first two underground nuclear tests — 22 September 1969 and 27 October 1975 — and has been inactive ever since. The two active test areas — zone A (41° 42' N, 88° 22' E) and zone C (41° 34' N, 88° 41' E) — have been in use since 17 October 1976 and 14 October 1978 respectively. Zones A and C cover approximately 200 square kilometers of the 100,000 square kilometer test site.

In addition to revealing the geographic layout of the Chinese test site, the refined seismic locations provided greater insight into the functionality of the two active test zones. Figures 8 and 9 contain three dimensional plots that combine seismic location estimates with the refined seismic yield estimates of Chinese underground nuclear tests.[31] The locations are plotted onto a UTM grid where the x-axis represents Easting and the y-axis represents Northing. The z-axis logarithmically represents the nuclear yield.

Figure 8 used the ISC/NEIS locations for the Chinese underground nuclear tests while Figure 9 used the refined JED locations for the same tests. As illustrated by the degree of scatter in the plot, Figure 8 provided little information on Chinese nuclear testing patterns. In contrast, Figure 9 clearly resolved the three test zones used for underground nuclear testing (zones A-C), revealing two operational relationships between the yield and location of Chinese nuclear tests.

Figure 9 shows that the active tunnel test area, zone A, has been used exclusively for low-yield tests (< 10 kt). The graph also shows that all underground tests with yields greater than 10 kilotons are conducted exclusively in the vertical shaft test area (zone C).[32] This pattern suggests that the Kizil Tagh mountain range in zone A is topographically or operationally unsuitable for tunnel tests at medium to high nuclear yields.

The operational relationship between yield and test zone provides a limited ability to anticipate the yield range of future Chinese tests through the remote observation of large-scale testing preparations in either zone.[33] The testing pattern also provides an additional verification mechanism to check for gross errors in preliminary seismic yield estimates made shortly after a nuclear test has occurred.
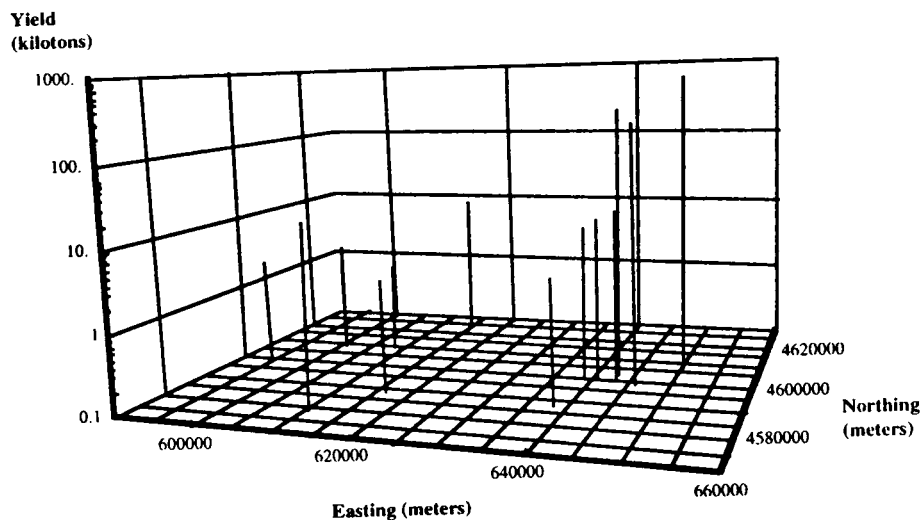
**Yield
(kilotons)**

Figure 8: Yield of Chinese underground tests in relation to ISC/NEIS location estimates (in UTM coordinates).
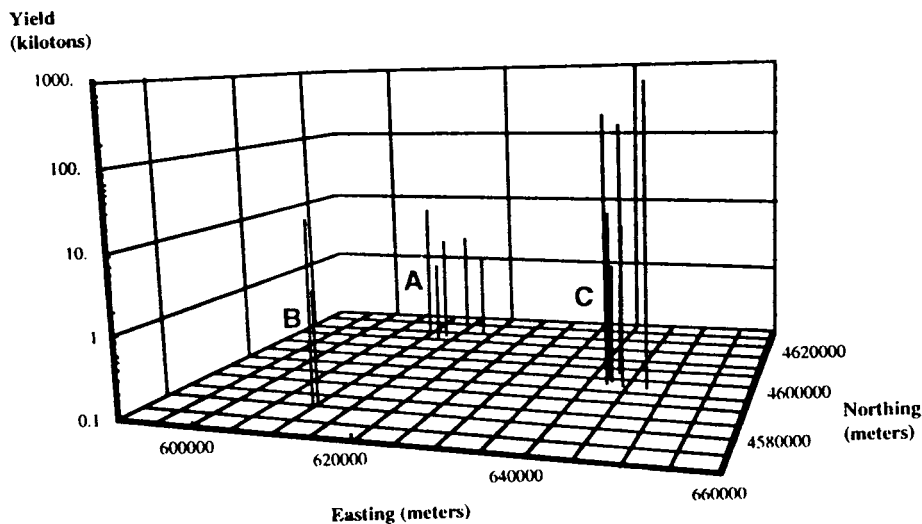
**Yield
(kilotons)**

Figure 9: Yield of Chinese underground tests in relation to JED location estimates (in UTM coordinates).

CONCLUSIONS AND IMPLICATIONS

The application of the JED with the image-derived locations for the 3 October 1984 and 27 June 1973 tests resulted in more accurate seismic location estimates for all Chinese nuclear tests reported in the ISC and NEIS bulletins through 1992. The convergence of the tests to four distinct zones provided valuable information on the layout and functionality of the test site. The increased understanding of past testing activities was subsequently used to assist the forecasting and rapid assessment of Chinese nuclear tests in 1992 and 1993.[34]

In the future, the results from this study can be used to assist the acquisition and interpretation of more recent commercial satellite images of the Chinese test site. Ongoing test preparations in either of the two active test zones could be identifiable in new satellite images of the area. For future Chinese nuclear tests, the arrival-time corrections generated by the JED for seismic stations worldwide could be used to reduce the systematic location error in real time. A refined seismic location estimate obtained shortly after a nuclear test could then be used to target satellite sensors quickly and accurately for post-test image acquisitions.

The JED results showed how large the systematic and random location errors can be. As shown in Figures 6 and 7, the errors were largest for weak seismic events (m_b < 5.0) generated by underground tests of a few kilotons or atmospheric tests of a few megatons.[35] The maximum systematic bias was 55 km and the maximum ellipse area was 2120 square kilometers (see Table D.1). The magnitude of the location errors for weak seismic events demonstrates the desirability of non-seismic approaches such as satellite remote sensing for reducing the search area. The need for non-seismic approaches still applies to the Chinese test site as well despite the JED results. Although the JED reduced the systematic location errors, it did not eliminate such errors. Consequently, some of the refined seismic location ellipses for the Chinese nuclear tests listed in Appendix D may not overlap with the actual location of the detonation point. Such discrepancies between JED location estimates and actual ground zero positions have been found at the Kazakhstan test site, averaging 1.2 kilometers compared to an average error ellipse dimension of 0.7 km.[36] If the actual ground zero positions of all Chinese nuclear tests are ever obtained in the future, a similar comparison could be made to evaluate the JED results listed in Table 2 and Appendix D.

Implications for CTB Verification

In conjunction with studies of other nuclear test sites, the remote sensing study of the Chinese test site demonstrated the utility of existing commercial imaging satellites for monitoring ongoing nuclear testing programs.[37] However, it did not establish the utility of existing commercial-imaging satellites as a significant component of a CTB verification regime. While routine nuclear testing can be monitored through commercial satellite imaging, it does not necessarily follow that clandestine tests can be observed reliably in the same way.[38]

Using unambiguous seismic data to establish the general vicinity of a test site, existing commercial-imaging satellites can reveal numerous facts about nuclear testing programs. However, it is not readily evident that the same satellites could provide comparable facts in an environment where low-yield tests (< 1 kiloton) generate ambiguous seismic signals, where camouflage, concealment, and deception are vigorously applied, and where tests could be conducted anywhere. Thus, in the near term, it would be prudent to continue the use of existing commercial remote-sensing satellites for monitoring known nuclear testing programs and defer the task of test ban verification to higher resolution sensors on intelligence satellites and forthcoming commercial imaging satellites. Scheduled for launch over the next 1-2 years, these new commercial satellites will be designed to acquire panchromatic images at a 1-3 meter ground sample distance and multispectral images in the visible and near infrared at a 4 meter ground sample distance.[39] Such high-resolution imagery has the potential to be more useful for test ban verification, since it can provide more detailed spatial and spectral information on small-scale activities and explosive effects that presently cannot be found in ALMAZ, Landsat, LFC, and SPOT imagery.

If a comprehensive test ban is enacted in the next few years, the task of accurately locating weak seismic events in near real time will increase in importance and the verification role of high-resolution satellite imaging is likely to increase accordingly. The principal role of such imaging would be to narrow down the search for an epicenter from an area of a few thousand square kilometers to an area of a few tens of square kilometers. Such an areal reduction is essential not only for effectively executing on-site inspections,[40] but also for systematically controlling the seismic false-alarm rate. If high-resolution images did not show human activity or infrastructure in the vicinity of an epicenter, an ambiguous seismic event could be safely attributed to natural causes.

Old satellite images, post-event images, and databases of JED arrival time corrections for stations worldwide are potential sources for reducing the

inaccuracies associated with seismic location estimates. This study demonstrated how satellite imagery and seismic data can be combined to locate Chinese detonation points. The technical challenge for a CTB verification regime will be not only to enhance the quality of the synthesized data, but also to implement algorithms that speed up the entire analysis process.

APPENDIX A: IMAGE PROCESSING STEPS FOR CREATING AN LFC-MSS RATIO IMAGE FOR CHANGE DETECTION

The Landsat-1 MSS image consists of four spectral bands that cover the visible and near infrared portions of the electromagnetic spectrum (see Table A.1). Using the Landsat-1 sensor calibration equations and an enhanced dark-object scattering technique for estimating the amount of atmospheric scattering, each MSS band was converted to radiance values and the scattering component in each band was removed:[41]

$$L_i = \alpha_i D_i - \beta_i \qquad \text{(A-1)}$$

$$\beta_i = \left(\frac{\lambda_4}{\lambda_i}\right)^4 L_{a4} \qquad \text{(A-2)}$$

where

L_i – radiance (mW sr^{-1} cm^{-2})
D_i – digital number
α_i – sensor gain (mW sr^{-1} cm^{-2})
β_i – atmospheric scattering (mW sr^{-1} cm^{-2})
λ_4 – wavelength of MSS Band 4
λ_i – wavelength of MSS Band i
L_{a4} – atmospheric scattering in MSS Band 4

The enhanced dark-object scattering technique models scattering as a function of wavelength and uses the scattering magnitude in one band to calculate the amount of scattering in the other bands. In this case, Rayleigh scattering (λ^{-4}) was assumed to be the dominant phenomenon given the very clear atmospheric conditions in the image. The scattering in MSS Band 4 was measured directly from shadow pixels in the band. These pixels were found to contain negligible skylight reflectance and radiance from nearby ground areas, as indicated by the observed absence of surface structures in these pixels. As a result, the radiance values inside the shadow pixels represented only the radiance due to atmospheric scattering. Table A.2 shows the value of the sensor gain and scattering component calculated using equation (A-2) for each of the MSS bands.

After performing the radiometric conversion and atmospheric correction, the three bands that covered portions of the visible part of the electromagnetic spectrum — MSS Bands 4-6 — were added together to create a panchromatic band. This synthetic band was needed in order to digitally compare the MSS data with the LFC panchromatic orthoimage. However, before this could be done, the MSS panchromatic band had to be geometrically registered to the LFC orthoimage.

The MSS panchromatic band was registered to the northwest quadrant of the LFC orthoimage by selecting nineteen tie points that were identifiable in both images, calculating the coefficients of the second-order polynomial transformations (equations A-3 and A-4) through least squares minimization, applying the geometric transformations, and resampling the image to a 50 meter orthoimage grid through bilinear interpolation. All of the tie points were registered to subpixel accuracy.

$$x' = C_1 + C_2x + C_3y + C_4x^2 + C_5y^2 + C_6xy \qquad \text{(A-3)}$$
$$y' = C_7 + C_8x + C_9y + C_{10}x^2 + C_{11}y^2 + C_{12}xy \qquad \text{(A-4)}$$

where

x' – registered x position
y' – registered y position
x – unregistered x position
y – unregistered y position
C_i – constants

The registered MSS panchromatic band was then digitally merged with the LFC orthoimage through temporal band ratioing. The dark object scattering technique was applied to the LFC orthoimage as part of the operation:[42]

$$\theta = \tan^{-1}\left(\frac{L_{r\ mss}}{L_{r\ lfc} - L_{s\ lfc}} \right) \qquad \text{(A-5)}$$

where

θ – arctangent of ratio (radians)
$L_{r\ mss}$ – radiance in MSS synthetic band
$L_{r\ lfc}$ – radiance in LFC orthoimage
$L_{s\ lfc}$ – atmospheric scattering in LFC orthoimage

The angle, θ, had a range of 0 to $\pi/2$ and was rescaled from 0 to 255. The ratio image depicted the changes in the surface reflectivity. Pixels of little or no change were shown in medium tones of gray. Surface changes were depicted either as dark or light pixels where the magnitude of the change increased as the digital number (DN) approached 0 (θ = 0 radians) or 255 (θ = $\pi/2$ radians). The magnitude of the change corresponded with the angular separation in the two-dimensional feature space between the line connecting the pixel of interest with the origin and the regression line that fit the pixels representing no surface change (see Figure A.1).

Table A.1: Spectral capability and instantaneous field of view (IFOV) of Landsat-1 MSS.

Spectral Band	Spectral Range (μm)	IFOV
Band 4 (green)	0.50-0.60	79 m
Band 5 (red)	0.60-0.70	79 m
Band 6 (red-near IR)	0.70-0.80	79 m
Band 7 (near IR)	0.80-1.10	79 m

Table A.2: Sensor gain and atmospheric scattering values for 4 Oct 1972 Landsat-1 MSS scene.

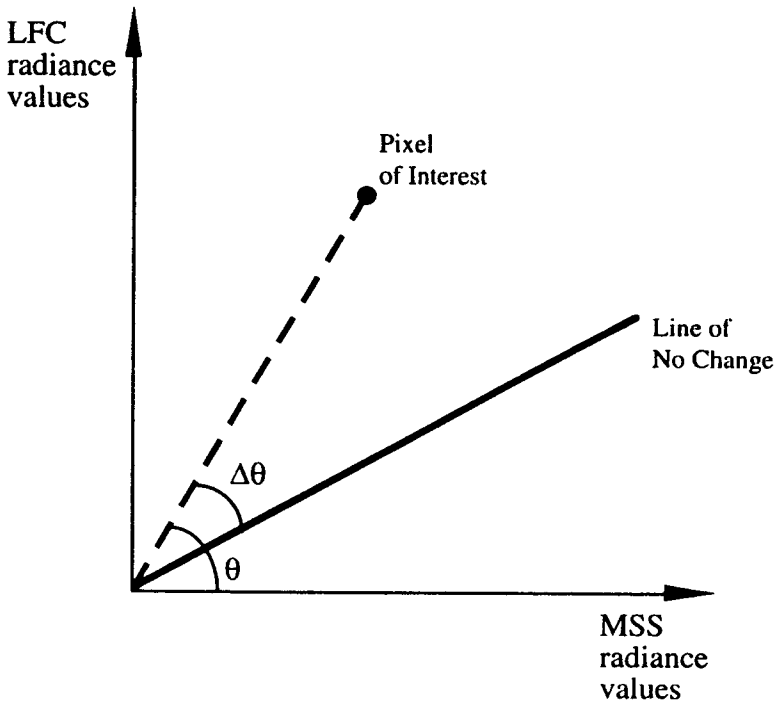| MSS Band	α (mW sr^{-1} cm^{-2})	β (mW sr^{-1} cm^{-2})
Band 4	0.01938	0.3710
Band 5	0.01563	0.1903
Band 6	0.01386	0.1072
Band 7	0.06349	0.0416

Figure A.1: Change quantified by angular separation in feature space.

APPENDIX B: LINKING A SURFACE BLEMISH IN THE LFC ORTHOIMAGE TO A CHINESE UNDERGROUND NUCLEAR TEST DESCRIBED IN Y. CHE'S TECHNICAL PAPER

The July 1987 issue of *Shuiwendizhi Gongchengdizhi* (Hydrology and Engineering Geology) contains a technical paper by Yongtai Che on the changes in local ground water levels caused by two underground nuclear explosions at the Chinese nuclear test site.[43] The paper contains detailed hydrological and geological information on the test site, but does not include information on the nuclear yields, detonation dates, or geographic locations of the two underground tests.[44] The medium of detonation, the approximate depth of burial, and the relative location of the two detonation points are the only details provided in the paper.

Both of the described tests were conducted in deep vertical shafts below the water table. Explosion I was detonated in granite at a depth of "about 280 meters." Explosion II was detonated in metamorphic sandstone at a depth of "more than 200 meters." The relative location of each detonation point was shown in a small-scale, geological map of the test zone (see Figure B.1). The scale of the map was provided, but the geographic coordinates and the type of map projection were not.

To determine exactly what portion of the test site was described in the 1:115,000 scale map, a search was conducted within the LFC orthoimage for the boundaries of the geological features shown in Figure B.1.[45] This search yielded five point features that could be identified in both the map and the LFC orthoimage. These tie points were used to calculate the coefficients of an affine transformation. The geometric transformation was then applied, registering the map onto the LFC orthoimage:

$$x' = C_1 + C_2 x + C_3 y \qquad \text{(B-1)}$$
$$y' = C_4 + C_5 x + C_6 y \qquad \text{(B-2)}$$

where

x' – registered x position
y' – registered y position
x – unregistered x position
y – unregistered y position
C_i – constants

Plate B.1 shows the quality of the fit. In the upper half of the map, the boundaries of the metamorphic sandy conglomerates and the aeolian material
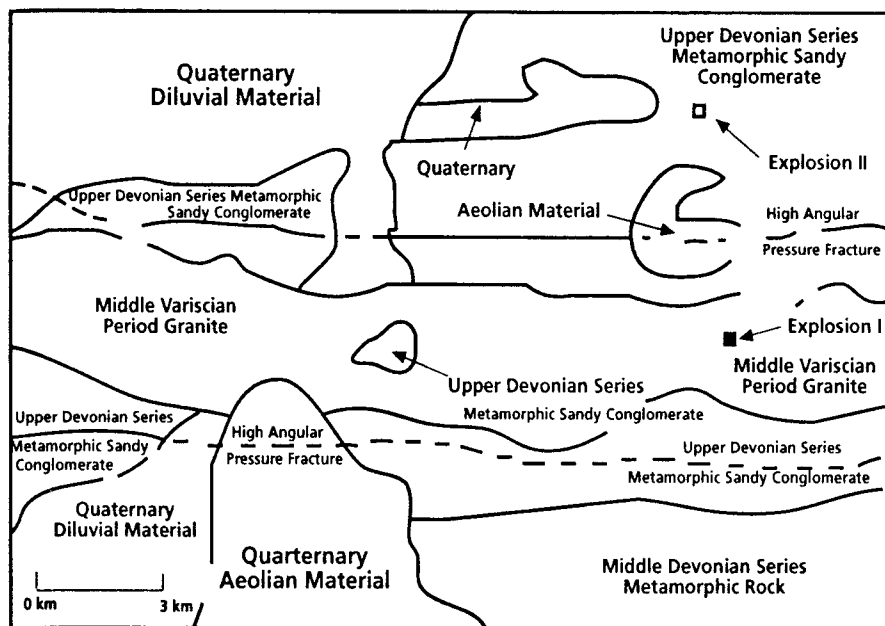
Figure B.1: 1:115,000 geological map containing two explosion points.

coincide with the borders in the orthoimage. In the lower half, the eastern border of aeolian material traces the textural boundary with the metamorphic sandy conglomerate and metamorphic rock. Portions of the map do not correspond exactly with the features in the orthoimage due to the low number of identifiable tie points as well as the unknown geological and cartographic accuracy of the map. Nonetheless, the common features between the map and orthoimage were sufficient to conclude that both depict the same area on the ground. Thus, Plate B.1 provides the absolute map orientation that was omitted in Che's paper.

Plate B.1 includes the projected location of Explosions I and II described by Che. The location of Explosion II overlaps with the upper left extremity of the large blemish that was identified in the ratio image shown in Plate 1. The overlap links a known detonation point (Explosion II) to the detected surface blemish. This link reinforces the inference of the surface blemish shown in Plate 1 as the detonation point for a vertical shaft nuclear test. The additional factors described in the third section made it possible to go one step further and deduce that the surface blemish contained the 3 October 1984 detonation point.
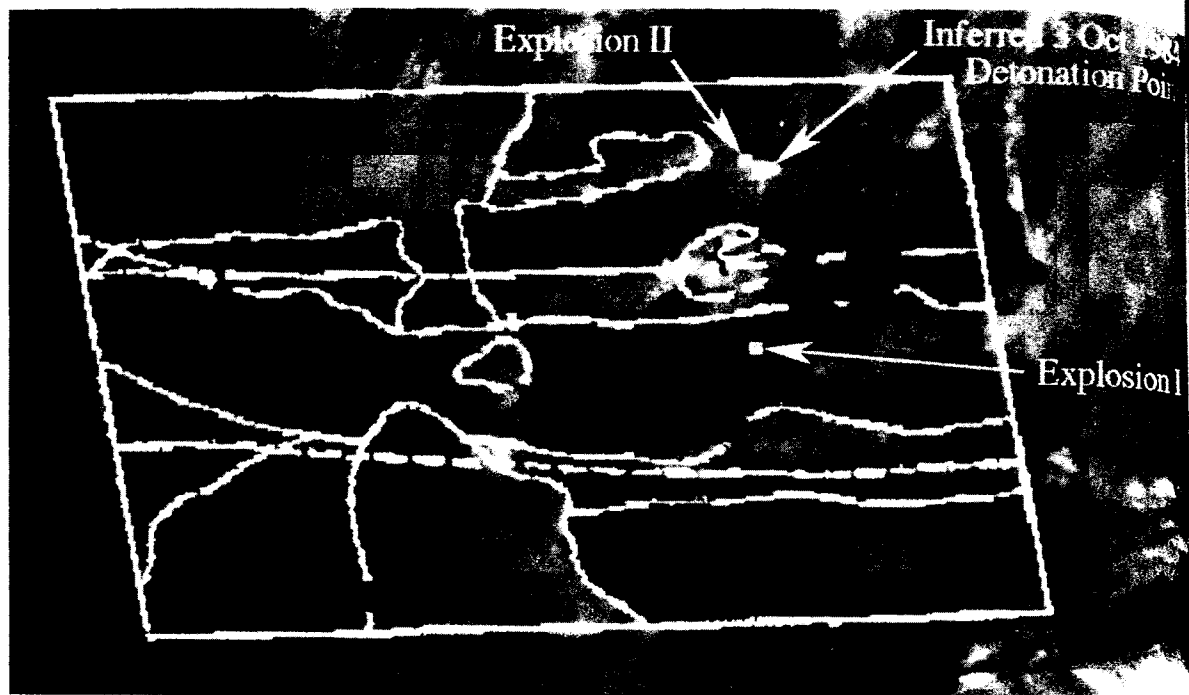
Plate B.1: Che's geological map (Figure B.1) registered to LFC orthoimage subscene with
tie points denoted as red crosses. Image extent: 24.50 km x 14.10 km.
See Color Plate I at back of journal

APPENDIX C: COMPARISON OF JED LOCATIONS OBTAINED IN THIS STUDY WITH JED LOCATIONS OBTAINED BY THE UK ATOMIC WEAPONS ESTABLISHMENT (AWE)

Figures C.1 and C.2 compare the JED results obtained in this study with the JED results obtained by Douglas *et al.* of the UK Atomic Weapons Establishment (AWE). Figure C.1 compares the locations for the underground tests in zones A-C and Figure C.2 compares the locations for the high-yield, atmospheric tests in zone D (see Figure 2 for test site layout). Only the locations of Chinese tests up to 1988 were plotted onto the graphs since the AWE study did not include Chinese tests that followed the 29 September 1988 explosion. The AWE locations in Figure C.1 are labeled by the month and the year of the test if more than one underground test was conducted in the calendar year. The AWE locations in Figure C.2 are labeled by the year of the test.

The positional differences between the JED results listed in Table 2 and the JED results from AWE are shown by the connecting lines that were plotted onto the graphs at the same scale. For the underground tests, the differences shown in Figure C.1 are minor with the AWE locations overlapping the respective 95 percent confidence error ellipses generated by this study (see Table D.1). The similar results can be attributed to both studies' use of the 3 October 1984 test as a reference event.

The AWE study used the 6 October 1983 test and the 3 October 1984 test as reference events. It selected these two tests based on a simple process of elimination done by J. Matzko of the US Geological Survey. Using the Figure B.1 map with approximate geographic coordinates inserted by Matzko and the ISC/NEIS seismic data, Matzko identified the 6 October 1983 and 3 October 1984 tests as "Possible Explosion I" and "Possible Explosion II" respectively.[46] The AWE study relied on Matzko's educated guess, which was established by this study as correct. The LFC-MSS image analysis linked Explosion II to the 3 October 1984 test (see Plate 1 and Appendix B) and the subsequent JED results overlay the Explosion I location with the 6 October 1983 location obtained from this study (see Figure C.1).

For the high-yield, atmospheric tests in zone D, the JED locations from this study differ substantially from the JED locations from AWE (see Figure C.2). The differences can be attributed to the use of a JED reference event in zone D for this study, but not for the AWE study. The 27 June 1973 test served as the local calibration shot for the other weak seismic events generated by atmospheric explosions. Consequently, its use in the JED reduced the location errors that were specific to zone D, an area removed from the underground testing zones (see Figure 2).
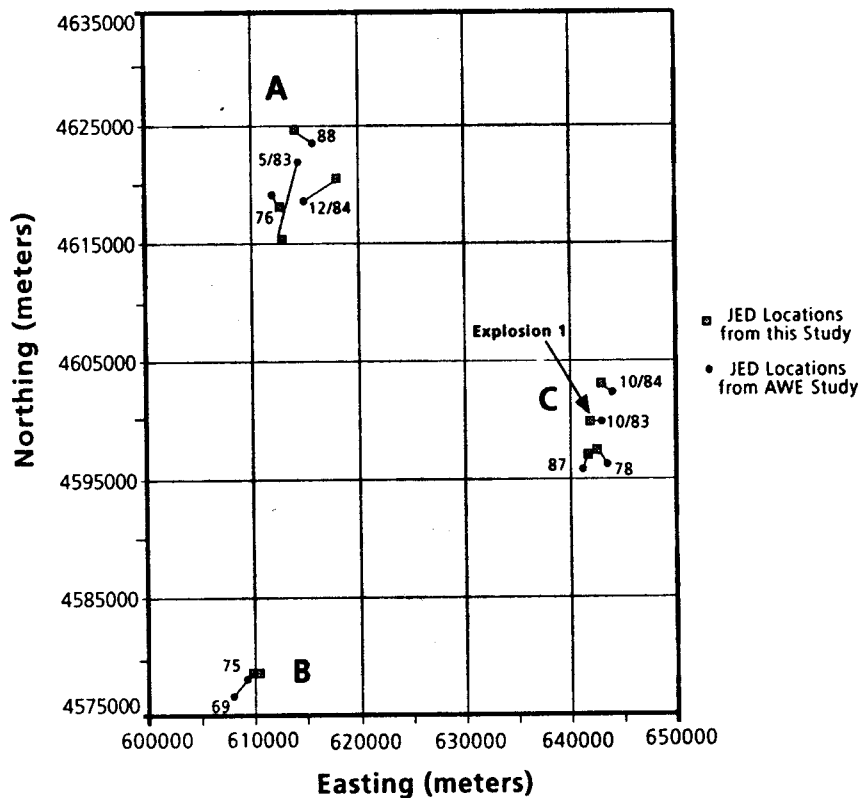
Figure C.1: Comparison of JED location estimates from this study and from the AWE study for Chinese underground tests in zones A-C (UTM grid units).
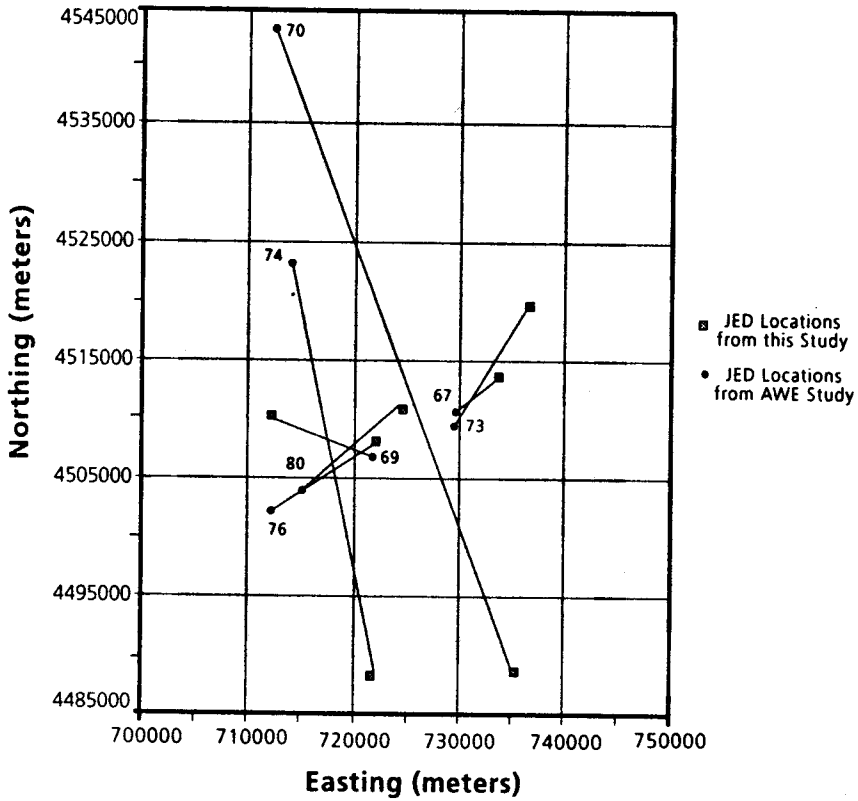
Figure C.2: Comparison of JED location estimates from this study and from the AWE study for Chinese atmospheric tests in zone D (UTM grid units).

APPENDIX D: JED TECHNICAL RESULTS ON CHINESE NUCLEAR TESTS

Table D.1 lists the results from the Joint Epicenter Determination. For each test in the dataset, the table shows the size, eccentricity, and orientation of the 95 percent confidence error ellipse.[47] It also provides the magnitude and direction of the systematic location error with respect to the ISC/NEIS location estimates. No ellipse parameters are provided for the 27 June 1973 and the 3 October 1984 explosions as these tests were located in commercial satellite images and used as fixed reference points in the JED.

Table D.1: JED results on nuclear explosions at the Chinese test site.

Date	m_b	Ellipse Area (km²)	Semi major Axis (km)	Semi minor Axis (km)	Ellipse Orientation Angle[a]	Magnitude of Error Vector (km)	Direction of Error Vector[b]
17 Jun 1967	4.7	42.77	5.11	3.56	151.98°	32.31	101.02°
22 Sep 1969	5.2	11.36	2.56	1.89	140.06°	3.08	340.66°
29 Sep 1969	4.5	2117.97	159.39	5.57	169.06°	18.20	89.28°
14 Oct 1970	4.6	219.44	11.11	8.25	155.88°	54.82	144.08°
27 Jun 1973	4.8	0.00	0.00	0.00	0.00°	18.93	34.98°
17 Jun 1974	4.5	888.59	28.77	12.93	5.56°	3.96	206.29°
27 Oct 1975	5.0	23.92	4.33	2.34	156.85°	8.68	225.08°
17 Oct 1976	4.9	16.10	3.00	2.23	149.35°	15.34	60.44°
17 Nov 1976	4.6	87.41	12.35	3.00	141.44°	9.71	196.46°
14 Oct 1978	4.9	16.19	3.00	2.34	136.28°	12.51	24.31°
16 Oct 1980	4.4	87.54	9.57	3.90	144.53°	45.71	218.77°
04 May 1983	4.5	181.23	19.21	4.01	16.67°	7.29	41.72°
06 Oct 1983	5.5	6.23	2.11	1.22	36.73°	.97	329.82°
03 Oct 1984	5.4	0.00	0.00	0.00	0.00°	5.53	49.95°
19 Dec 1984	4.7	14.59	3.00	2.00	140.58°	21.44	52.56°
05 Jun 1987	6.2	5.64	2.00	1.22	42.06°	8.99	198.26°
29 Sep 1988	4.6	29.82	4.89	2.56	136.34°	33.61	34.78°
26 May 1990	5.4	6.77	2.22	1.34	31.68°	3.38	16.20°
16 Aug 1990	6.2	5.52	2.00	1.22	37.41°	1.11	232.59°
21 May 1992	6.6	6.01	2.11	1.22	38.96°	10.13	197.22°
25 Sep 1992	5.1	8.97	2.45	1.56	40.39°	6.67	222.29°

a. Orientation angle measured in clockwise direction from the UTM northing axis.
b. Direction of error vector measured in clockwise direction from the UTM northing axis.

ACKNOWLEDGEMENTS

NOTES AND REFERENCES

1.   Vipin Gupta, "Future Chinese Nuclear Tests on the Horizon," *Trust & Verify* 30, July/August 1992, pp. 2-3 (Presented at the 4th International Summer School on Science and World Affairs, August 28, 1992, Shanghai); R. Jeffrey Smith, "China Planning a Nuclear Test, US Aides Say: Nations Pressure Beijing to Observe Moratorium," *Washington Post*, September 17, 1993, p. A1.

2.   John Matzko, "Geology of the Chinese Nuclear Test Site near Lop Nor, Xinjiang Uygur Autonomous Region, China," *Engineering Geology* 36, 1994, pp. 173-181 (Presented at the 14th Annual PL/DARPA Seismic Research Symposium, September 16-18, 1992, Tucson, Arizona).

3.   Robert Norris, Andrew Burrows, and Richard Fieldhouse, *Nuclear Weapons Databook volume V: British, French, and Chinese Nuclear Weapons* (Boulder: Westview Press, 1994), pp. 350-356.

4.   John Murphy, "Yield Estimation and Bias at the Chinese Lop Nor Test Site," pp. 1-21 (Presented at the 14th Annual PL/DARPA Seismic Research Symposium, September 18, 1992, Tucson, Arizona).

5.   The P-wave is a compressional body wave that travels through the Earth's crust and mantle.

6.   The AWE study also refined the body-wave magnitudes (m_b) of Chinese nuclear tests recorded in the ISC bulletins through 1988. A. Douglas, P. Marshall, and K. Jones, "Body-Wave Magnitudes and Locations of Explosions at the Chinese Test Site, 1967-1989," AWE Report No. O 12/93, December 1993, pp. 1-19.

7.   Vipin Gupta, "Assessment of the Chinese Nuclear Test Site near Lop Nor," *Jane's Intelligence Review* 5 (8), August 1993, pp. 378-381. Vipin Gupta and Philip McNab, "Sleuthing from Home," *The Bulletin of the Atomic Scientists* 49 (10), December 1993, pp. 44-47. Vipin Gupta, "The Status of Chinese Nuclear Weapons Testing," *Jane's Intelligence Review* 7 (1), January 1994, pp. 31-35. Vipin Gupta, *A Remote Sensing and Photogrammetric Study of the Chinese Nuclear Test Site*, PhD thesis (University of London, February 1995), pp. 1-264.

8.   Gupta and McNab, "Sleuthing from Home," pp. 44-47. Smith, "China Planning a Nuclear Test, US Aides Say: Nations Pressure Beijing to Observe Moratorium," p. A1.

9. For example, high-resolution imagery acquired by the Russian KVR-1000 camera and processed to a 2-meter ground sample distance (GSD) cost US $13 per square kilometer in 1993. Thus, the cost for KVR-1000 imagery of the entire Chinese test site (100,000 sq. km) would be US $1,300,000 assuming no bulk percentage discount was offered. The cost for KVR-1000 imagery of only the active portions of the Chinese test site (200 sq. km) would be substantially less — US $6,000.

10. Norris, Burrows, and Fieldhouse, *Nuclear Weapons Data book Volume V: British, French, and Chinese Nuclear Weapons*, pp. 420-422.

11. The Chinese underground test on 5 October 1982 was not reported in the ISC/NEIS bulletins, although it was detected by a few seismic stations.

12. Scaled height of burst (H_s) is defined as $H/Y^{1/3}$ where
    H - actual height of burst
    Y - nuclear yield

13. The yields for the atmospheric tests were published in Norris, Burrows, and Fieldhouse, *Nuclear Weapons Databook Volume V: British, French, and Chinese Nuclear Weapons*, pp. 420-422. The yields for the underground tests were published in Gupta, "The Status of Chinese Nuclear Weapons Testing," p. 32.

14. H. Jeffreys and K. Bullen, "Seismological Tables," British Association for the Advancement of Science, Gray-Milne Trust, 1967.

15. B. Bolt, "The Revision of Earthquake Epicenters, Focal Depths, and Origin-Time Using a High Speed Computer," *Geophys. J. Roy. Astron. Soc.* 3, 1960, pp. 434–440. B. Bolt, "Earthquake Location for Small Networks Using the Generalized Inverse Matrix," *Bulletin of the Seismological Society of America* 60, 1970, pp. 1823–1828.

16. Unfortunately, nuclear tests — particularly low-yield tests — are often not detected under such preferred circumstances. Ola Dahlman and Hans Israelson, *Monitoring Underground Nuclear Explosions* (Amsterdam: Elsevier Scientific Publishing, 1977), p. 189.

17. Dahlman and Israelson, *Monitoring Underground Nuclear Explosions*, p. 176.

18. Roger Clark and John Baruch, "Verification of a Comprehensive Test Ban," in Frank Barnaby, ed., *A Handbook on Verification Procedures* (London: MacMillan Press, 1990), p. 88.

19. Alan Douglas, "Joint Epicenter Determination," *Nature* 215 (5096), July 1, 1967, pp. 47–48.

20. The detonation dates for the four underground nuclear tests were not provided, however. Yan Lu, "Physical Geological Reactions to Underground Nuclear Explosions," *Shuiwendizhi Gongchengdizhi* (5), September 1980, pp. 13-16. Jinli Wang and Tiezhong Xu, "A Preliminary Study of Abnormal Movement of Ground Water Influenced by an Underground Nuclear Explosion," *Shuiwendizhi Gongchengdizhi* (5), September 1983, pp. 33-36. Yongtai Che, "Response of Ground Water Level in Wells to Underground Explosion," *Shuiwendizhi Gongchengdizhi* (4), July 1987, pp. 7-12.

21. All distances were measured in Universal Transverse Mercator grid coordinates.

22. Surface spallation from a vertical shaft test could also increase albedo. However, for vertical shaft tests, it is not possible to discriminate between surface effects caused by test preparation and the explosion unless an additional image is acquired shortly before detonation.

23. The SPOT-1 scene clearly showed paved roads at the site. Gupta, "The Status of Chinese Nuclear Weapons Testing," p. 34.

24. US Congress, Office of Technology Assessment, *The Containment of Underground Nuclear Explosions,* OTA-ISC-414 (Washington, DC: US Government Printing Office, October 1989), pp. 11-27.

25. The prevailing winds at Lop Nor flow from the northeast with wind speeds of 65-77 km per hour sweeping through the region an average of 80 days per year. Shu Peng Chen, ed., *Atlas of Geoscience Analyses of Landsat Imagery in China* (Beijing: Science Press), 1986, p. 178.

26. Fanned configurations have been observed at the US Nevada Test Site. Thomas B. Cochran, William Arkin, Robert S. Norris, and Milton M. Hoenig, *Nuclear Weapons Databook Volume II: US Nuclear Warhead Production* (Cambridge: Ballinger Publishing, 1987), p. 48.

27. In seismology, distances are expressed as the angle at the center of the Earth that subtends the arc connecting the seismic source to the receiving station.

28. Gupta, "Assessment of the Chinese Nuclear Test Site near Lop Nor," pp. 379-380.

29. Douglas, Marshall, and Jones, "Body-Wave Magnitudes and Locations of Explosions at the Chinese Test Site, 1967-1989," pp. 4, 16.

30. Dahlman and Israelson, *Monitoring Underground Nuclear Explosions,* p. 189.

31. With the exception of the tests on 22 September 1969 and 29 September 1988, the refined yield estimates in Figures 8 and 9 were derived from the seismic analysis by Murphy (Murphy, "Yield Estimation and Bias at the Chinese Lop Nor Test Site," pp. 1–21). The yield of the 22 September 1969 test was obtained from Yang (Yang Fujia, "An Informal Talk on the 21 May 1992 Nuclear Test," International Summer School on Science and World Affairs, Fudan University, 28 August 1992). The yield of the 29 September 1988 test was obtained from Clark (Roger Clark, "Report on L_g–based Yield Estimation of Two Chinese Nuclear Tests — 29 September 1988 and 5 October 1993," 4 November 1993, p. 1). See Table 1 for the list of yields from Chinese underground nuclear tests through 1992.

32. Before the eastern zone was operational, China did conduct one underground nuclear test (22 September 1969) in zone B which reportedly had a yield of 19.2 kilotons (see Table 1).

33. Gupta, "Future Chinese Nuclear Tests on the Horizon," pp. 2-3. Gupta, "The Status of Chinese Nuclear Weapons Testing," pp. 31-35.

34. Gupta, "Future Chinese Nuclear Tests on the Horizon," pp. 2-3. Gupta and McNab, "Sleuthing from Home," pp. 44-47.

35. For studies of weak seismic events that apply satellite remote sensing and seismology, multimegaton atmospheric tests at low scaled heights of burst can be used as substitutes for underground tests of a few kilotons. The atmospheric tests are preferable because it is easier to detect and identify surface remnants from an atmospheric test in a satellite image.
    For studies on nuclear test ban verification, it may be worthwhile to investigate old atmospheric explosions that were detected seismically. Satellite imagery can be used to locate the detonation points. Seismic location errors can be measured with respect to the image-derived locations and the seismic capability for pinpointing weak events in the vicinity of old test sites can be assessed remotely.

36. C.H. Thurber, H.R. Quin, and P.G. Richards, "Accurate Locations of Nuclear Explosions in Balapan, Kazakhstan, 1987 to 1989," *Geophysical Research Letters* **20** (5), 5 March 1993, p. 401.

37. For remote sensing studies of the US Nevada Test Site, see Bhupendra Jasani, "Civil Observation Satellites and Arms Control Verification," Preliminary Report, Department of War Studies, King's College London, August 1992, pp. 65-69. Peter Zimmerman, "Study of the Nevada Test Site using Landsat Satellite," CSIS Report, 1993, pp. 1-9.

For remote sensing studies of the former Soviet test sites, see Ulf Ekblad and Hans-Ake Olsson, "Satellite Imagery Detection of Preparations for Underground Nuclear Explosions," FOA Report C 30560-9.4, Swedish Defense Research Establishment, Linköping, January 1990, pp. 1-18. William Leith and David Simpson, "Monitoring Underground Nuclear Tests," in Michael Krepon, Peter Zimmerman, Leonard Spector, and Mary Umberger, *Commercial Observation Satellites and International Security* (New York: St. Martin's Press, 1990), pp. 115-124. Johnny Skorve and John Skogan, "The NUPI Satellite Study of the Northern Underground Nuclear Test Area on Novaya Zemlya," NUPI Report No. 164, December 1992, pp. 1-51. Lynn Sykes, Jishu Deng, and Paul Lyubomirskiy, "Accurate Location of Nuclear Explosions at Azgir, Kazakhstan, from Satellite Images and Seismic Data: Implications for Monitoring Decoupled Explosions," *Geophysical Research Letters* **20** (18), 15 September 1993, pp. 1919-1922. Thurber *et al.*, "Accurate Locations of Nuclear Explosions in Balapan, Kazakhstan, 1987 to 1989," pp. 399-402. C.H. Thurber, H.R. Quin, and R. Saleh, "Catalog of Locations of Nuclear Explosions at Balapan, Kazakhstan, 1965 to 1985," submitted to *Bulletin of the Seismological Society of America*, 11 August 1993, pp. 1-13.

38. Vipin Gupta and John Hassard, "Space-based Electromagnetic Remote Sensing for Monitoring Nuclear Explosive Testing," accepted for publication in *Surveys in Geophysics*.

39. Some of these satellites will also be able to acquire high-resolution images of 15,000-20,000 sq km areas in a single flyover. For details on the technical capabilities of the new imaging satellites, see Vipin Gupta, "New Satellite Images for Sale," to be published in *International Security* **20** (1), Summer 1995.

40. Warren Heckrotte, "On-site Inspection to Check Compliance," in Jozef Goldblat and David Cox, *Nuclear Weapon Tests: Prohibition or Limitation* (New York: Oxford University Press, 1988), p. 255.

41. Charles Robinove, "Computation with Physical Values from Landsat Digital Data," *Photogrammetric Engineering and Remote Sensing* **48** (5), May 1982, pp. 781-784. Pat Chavez, "An Improved Dark-Object Subtraction Technique for Atmospheric Scattering Correction of Multispectral Data," *Remote Sensing of Environment* **24**, 1988, pp. 459-479.

42. For a discussion on the merits of temporal band ratioing for change detection, see Gupta, *A Remote Sensing and Photogrammetric Study of the Chinese Nuclear Test Site*, pp. 160-166. For a discussion on the importance of removing atmospheric scattering effects before ratioing, see R. Crippen, "The Dangers of Underestimating the Importance of Data Adjustments in Band Ratioing," *International Journal of Remote Sensing* **9** (4), 1988, pp. 767-776.

43. Che, "Response of Ground Water Level in Wells to Underground Explosion," pp. 7-12.

44. Although the detonation dates were not provided, the two underground nuclear tests must have taken place before July 1987 — the month and year the paper was published.

45. Through his geological analysis of the test site, J. Matzko narrowed down the search to a region that covered approximately two times the ground area covered in the map. Matzko, "Geology of the Chinese Nuclear Test Site near Lop Nor, Xinjiang Uygur Autonomous Region, China," pp. 173-181.

46. Matzko, "Geology of the Chinese Nuclear Test Site near Lop Nor, Xinjiang Uygur Autonomous Region, China," p. 176.

47. The eccentricity quantifies the shape of the ellipse and can be expressed as a function of the semimajor and semiminor axes:

where $\quad e = \sqrt{1 - b^2/a^2}$
    e – eccentricity
    a – semimajor axis
    b – semiminor axis
For an ellipse, $0 \le e < 1$.